Acta Biomaterialia 199 (2025) 193–201

Contents lists available at ScienceDirect

Acta Biomaterialia

journal homepage: www.elsevier.com/locate/actbio

Full length article

Insights into the osteosarcoma microenvironment: Multiscale analysis of structural and mineral heterogeneity

Francesca Rossi [a], Martyna Malgorzata Rydzyk [a], Luisa Barba [b], Emil Malucelli [a,*], Maria Elisabetta Federica Palamà [c], Chiara Gentili [c,d], Maddalena Mastrogiacomo [e,f], Alessia Cedola [g], Lucia Mancini [h], Murielle Salomé [i], Hiram Castillo-Michel [i], Davide Maria Donati [j,k], Marco Gambarotti [l], Enrico Lucarelli [m,1], Michela Fratini [g,n,1], Stefano Iotti [a,o,1]

[a] Department of Pharmacy and Biotechnology, University of Bologna, via San Donato 15, 40127, Bologna 33-40126, Italy
[b] CNR-IC, Area Science Park, SS14 km 163.5, Basovizza, Trieste 34142, Italy
[c] Department of Experimental Medicine, University of Genoa, Genova, Italy
[d] UO. Oncologia Cellulare-IRCCS Ospedale Policlinico San Martino, Genova, Italy
[e] Department of Internal Medicine and Medical Specialities (DIMI), University of Genoa, viale Benedetto XV 6, 16132 Genoa, Italy
[f] UO. Bioterapie-IRCCS Ospedale Policlinico San Martino, Largo Rosanna Benzi 10, 16132 Genoa, Italy
[g] Institute of Nanotechnology – CNR, c/o Dept of Physics, Sapienza University Piazzale Aldo Moro 5, Rome, Italy
[h] Department of Materials, Slovenian National Building and Civil Engineering Institute (ZAG), Dimičeva ulica 12, Ljubljana 1000, Slovenia
[i] ESRF, The European Synchrotron, 71 Avenue des Martyrs, CS40220, 38043, Grenoble CEDEX 9, France
[j] 3rd Orthopaedic and Traumatologic Clinic Prevalently Oncologic, IRCCS Istituto Ortopedico Rizzoli, Via Pupilli 1, Bologna 40136, Italy
[k] Department of Biomedical and Neuromotor Sciences (DIBINEM), Alma Mater Studiorum University of Bologna, Bologna 40126, Italy
[l] Department of Pathology, IRCCS, Istituto Ortopedico Rizzoli, Via Pupilli 1, Bologna 40136, Italy
[m] Osteoncology, Bone and Soft Tissue Sarcomas and Innovative Therapies Unit, IRCCS Istituto Ortopedico Rizzoli, Bologna, Italy
[n] Neuroimaging Laboratory, IRCCS Fondazione Santa Lucia, Via Ardeatina 306, 00179 Roma, Italy
[o] National Institute of Biostructures and Biosystems (NIBB), Rome 00136, Italy

ARTICLE INFO

Keywords:
Osteosarcoma
Biomineralization
XANES
Synchrotron-based X-ray diffraction
X-ray computed microtomography

ABSTRACT

Osteosarcoma (OS) is a malignant and heterogeneous disease that typically originates in the long bones of children and adolescents. It is characterized by the presence of immature cells having an aggressive phenotype and rapid uncontrolled proliferation. OS progression induces significant molecular and cellular changes locally within the bone, resulting in the development of an abnormal tumor microenvironment (TME). The OS TME plays a crucial role in tumor progression and development, however, the precise effects of OS on bone structure and mineralization still remain poorly understood. In this study, we examined the OS TME by analyzing samples from osteoblastic, parosteal, and periosteal osteosarcomas. Employing advanced synchrotron-based X-ray techniques, we performed a multiscale analysis to evaluate the structural and mineral complexity of tumor-affected bone. Our results revealed marked morphological differences among the osteosarcoma subtypes, while confirming that biomineralization remains active through the production of hydroxyapatite (HA). X-ray diffraction identified two distinct hydroxyapatite crystalline phases across all samples, suggesting a critical behavior of minerals in bone. Additionally, we observed that the bone mineral structure in periosteal and parosteal osteosarcomas exhibited crystal deformations along the c-axis, whereas the osteoblastic osteosarcoma displayed a mineral profile comparable to control bone. Micro-X-ray absorption near-edge spectroscopy revealed the occurrence of a dysregulated biomineralization in the parosteal and periosteal subtypes, marked by the presence of calcium compounds different from HA, in contrast to the mature mineral state found in the osteoblastic variant. These findings highlight the complexity of osteosarcoma repercussion on bone tissue, offering new insights into the interactions within the OS TME.

* Corresponding author.
E-mail address: emil.malucelli@unibo.it (E. Malucelli).
[1] Co-last authors.

https://doi.org/10.1016/j.actbio.2025.04.057
Received 16 December 2024; Received in revised form 28 April 2025; Accepted 30 April 2025
Available online 1 May 2025

Statement of Significance: This study investigates the tumor microenvironment (TME) of osteosarcoma (OS), a rare and aggressive bone cancer mainly affecting children and adolescents. Using advanced synchrotron-based X-ray techniques, we analyzed structural and mineral alterations in bone from three OS subtypes: osteoblastic, parosteal, and periosteal. The results reveal distinct subtype-specific differences in bone mineralization and crystallinity, highlighting the heterogeneity of OS and the pivotal role of its microenvironment in driving disease progression. This research contributes to our understanding of OS pathophysiology and provides foundation for future studies aimed at developing targeted therapies and improving diagnostic approaches.

1. Introduction

Osteosarcoma (OS) is the most common primary malignant bone tumor, mainly affecting adolescents and young adults [1]. It includes several sub-types, each having different phenotype and characteristics, therapeutic approaches, and outcome. OS is conventionally treated by multi-modal approaches that combine surgery with multi-agent chemotherapy. Unfortunately, the current treatment protocols are not effective for all patients where OS may recur locally or spread to vital organs. Therefore, the effectiveness of new therapeutic approaches is constantly investigated [2]. Recent efforts have focused on the characterization of the tumor micro-environment (TME) at a cellular level to identify potential new therapeutic targets and strategies [3–5]. The OS TME, which mainly includes bone, stromal, vascular, and immune cells, plays a crucial role in tumor progression and development through its dynamic interaction with OS cells [3,4,6,7]. However, the precise effects of osteosarcoma on bone structure and mineralization still remain poorly understood. To clarify the complex interplay between OS and its TME, bone has to be regarded as a dynamic system that operates across multiple length scales, from the molecular organization within collagen fibers and hydroxyapatite (HA) crystals to the macroscopic structure of the whole tissue [8–10]. In addition, the unique structural organization of bone displays fractal-like patterns, contributing to the complexity of the system [11,12]. Within this framework, the concept of criticality becomes relevant. Criticality refers to a state of a system that is on the verge of a transition, where it can shift between different states with small perturbations [13]. This concept has already been applied in other biological systems, notably the brain [14,15]. In the context of bone tissue, this could translate into rapid changes in mineralization, remodeling, or damage repair depending on factors such as injury or disease. To investigate the complex nature of osteosarcoma, it is necessary to employ advanced imaging and analytical techniques capable of probing bone structure across multiple scales. Synchrotron-radiation techniques offer the resolution and sensitivity required for such multiscale analyses, allowing to study both the macroscopic morphology and the atomic structure of bone tissue. In this study, three key synchrotron-based methods were used: X-ray Computed microtomography (XCmT), μ-X-ray Absorption Near-Edge Spectroscopy (μXANES) combined with X-ray Fluorescence Microscopy (XRFM), and X-ray Diffraction (XRD). XCmT offers high-resolution three-dimensional (3D) imaging of bone morphology. It enables the visualization of bone hierarchical structure and can detect morphological abnormalities caused by osteosarcoma at the microscopic level. μXANES provides insights into the molecular state of calcium within the bone tissue, and XRD gives detailed information about the bone minerals structure. These techniques are essential for understanding how tumor-induced disruptions alter bone mineralization. By integrating XCmT, μXANES, and XRD, this study aims to provide insights that enhance our understanding of how osteosarcoma affects bone's structural and mineral composition across three subtypes. In this study, we investigated high-grade osteosarcoma (HG-OS), parosteal osteosarcoma (PA-OS), and periosteal osteosarcoma (PE-OS), each differing in aggressiveness, location, histology, treatment, and prognosis. HG-OS is the most aggressive subtype and is treated with a combination of chemotherapy and surgery. In contrast, PE-OS, which is generally of intermediate aggressiveness, and PA-OS, which is low-grade, are both treated with surgery. Specifically, by offering detailed information on HA structure and bone mineral variations between control and tumor tissue, we provide valuable knowledge that could help clarify whether these differences influence tumor progression, ultimately contributing to improved patient outcomes.

2. Materials and methods

2.1. Bone samples

The bone specimens characterized in this study were collected from three osteosarcoma patients during elective surgery at Istituto Ortopedico Rizzoli (IOR) (Bologna, Italy), after Ethical Committee approval (744/2019/Sper/IOR) with written informed consent obtained from each patient. The three subjects had high-grade osteoblastic (HG-OS), parosteal (PA-OS) and periosteal (PE-OS) OS. A brief description of the patients in terms of age, gender and treatment is reported in Table S1. The selection of the regions of interest was performed by an expert osteosarcoma anatomopathologist in both tumoral and non-tumoral areas, and the specimens were preserved by freezing at -20 °C. Control bone tissue was specifically collected from non-tumoral margins to allow for intra-subject comparison. The region from which the control and tumoral samples were obtained has been indicated in Fig. 1. The HG-OS sample was extracted from a necrotic area of the trabecular distal femur in a patient who had undergone neoadjuvant chemotherapy, while PA-OS and PE-OS developed exophytic tumoral masses originating from the periosteum in the proximal femur and tibial bone respectively. While after chemotherapy, the HG-OS patient's sample exhibited 95 % necrosis, it remains unclear whether this resulted from the treatment or from the tumor's intrinsic aggressiveness. Histological evaluation of hematoxylin and eosin-stained sections from demineralized resected tissues was conducted for diagnostic purposes. These sections were taken from regions adjacent to those extracted for the multiscale analysis described in Section 2.4, as the analyzed samples could not be demineralized. In Fig. 1 D, a high-grade malignant epithelioid neoplasm producing malignant osteoid can be seen infiltrating the host bone trabeculae, consistent with high-grade osteoblastic osteosarcoma. Fig. 1 E shows a low-grade malignant spindle cell neoplasm associated with parallel-aligned bony trabeculae, characteristic of low-grade parosteal osteosarcoma. In Fig. 1 F, low-grade periosteal osteosarcoma is observed, composed of lobules with a low- to intermediate-grade cartilaginous component.

2.2. Sample processing

Bone resected tissues were collected from both tumor and control regions of each patient and preserved at -20°C. XCmT analysis was performed on the frozen samples as described in Section 2.4.1. Following this, the specimens underwent inclusion in poly-methyl methacrylate resin and sectioned using a diamond saw. A portion of the sections was stained for histological evaluation (described in Section 2.3), while the remaining ones underwent XRFM, μXANES, and XRD analysis (Sections 2.4.2 and 2.4.3). To provide a clearer overview of the sample processing workflow, a schematic representation is included in Fig. S1.

2.3. Histology

For multiscale analysis the excised tissues were de-hydrated and infiltrated with light-curing poly-methyl methacrylate (PMMA) resin (Technovit 7200VLC, Kulzer, Wehrheim, Germany) for 21 days with resin replaced every 7 days. Samples were polymerized by using the EXAKT 520 polymerization system (EXAKT Wehrheim, Bio-Optica, Italy, curing at 450 nm, T<40 °C). Serial sections with a thickness of 100–150 μm were cut using the EXAKT 310 CP cutting unit (EXAKT Wehrheim), then ground and polished with the EXAKT 400 CS micro grinding unit (EXAKT Wehrheim), to yield undecalcified sections with a final thickness of 20–30 μm. Some sections were stained for bright-field analysis with Stevenel's blue and van Gieson's picrofuchsin, where osteoid tissue appears blue and mineralized bone appears red. Images were acquired by AxioPhot microscope (Carl Zeiss, Oberkochen, Germany) (Fig. S2). The remaining sections were left unstained for X-ray synchrotron analysis.

2.4. X-ray synchrotron-based techniques

Synchrotron-based X-ray techniques, including XCmT, μXANES, and XRD, were used to conduct a multiscale analysis of resected human osteosarcoma tissues. XCmT enabled the characterization of bone morphology, μXANES provided molecular-level insights on the tissue, and XRD offered complementary structural information. The setup and methods used for each technique are described in the following sections.

2.4.1. X-ray computed microtomography

The morphological characterization of osteosarcoma bone samples was performed by propagation-based phase-contrast synchrotron X-ray computed microtomography (XCmT) at the SYRMEP (SYnchrotron Radiation for MEdical Physics) imaging beamline of the Elettra synchrotron facility in Trieste (Italy) [16].

Freshly collected bone samples were enveloped frozen (-20 °C) in Parafilm® and then mounted on the rotation stage for the acquisitions. The samples remained stable and did not move during the entire acquisition process. The investigations were performed by using a filtered white beam (filter: 1.0 mm Si plus 1.5 mm Al), corresponding to a mean X-ray energy of 27 keV, with the electron storage ring operating at 2.0 GeV [17]. A water-cooled, 2048 × 2048 pixels, 16-bit sCMOS camera (ORCA Flash 4.0, Hamamatsu, Japan) with a physical pixel size of 6.5 μm and equipped with a zoom system coupled to a 17 μm thick GGG scintillator screen was set at a fixed propagation distance from the sample. A set of 900 sample radiographs (projections) were acquired during a full rotation angle of 180° and with an exposure time/-projection of 2 s. Microtomographic scans were performed in different regions of the sample to account for intrasubject variability of tissue morphology. First, a volume of interest (64 mm^3) was scanned within each bone specimen using an effective pixel size of 2.0 × 2.0 μm^2 and a propagation distance of 200 mm. Then, in the same specimen, additional 1 to 3 volumes (8 mm^3) were imaged at higher spatial resolution with an effective pixel size of 0.9 × 0.9 μm^2 and a 150 mm propagation distance. This approach allowed for detailed multiscale imaging, enhancing resolution in specific regions of interest within the same sample. Volumetric datasets were reconstructed using the open-source software SYRMEP Tomo-Project (STP) [18,19]. The phase retrieve reconstruction was performed with optimized ratio between the delta coefficient and beta coefficient in order to better visualize the mineral component of bone tissue. The STP software has been used also to remove ring artefacts in the reconstructed axial slices. Reconstructed slices were

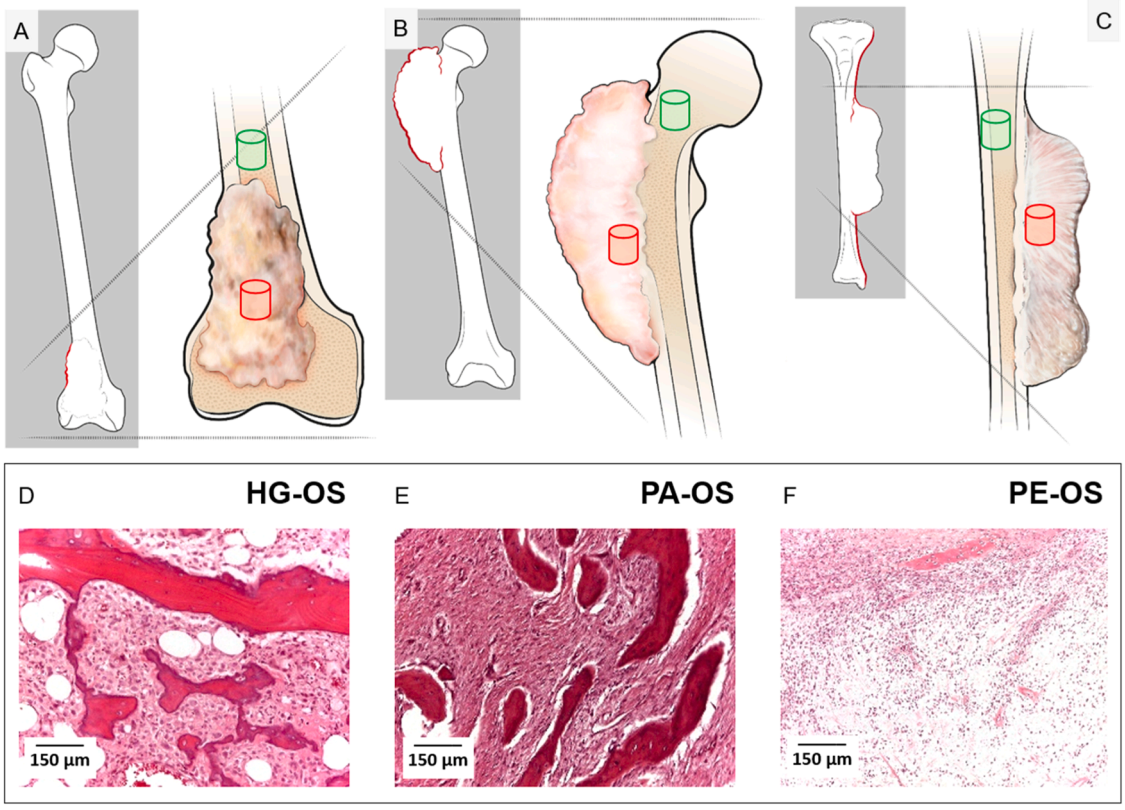

Fig. 1. Location of the isolated samples for HG-OS (A), PA-OS (B) and PE-OS (C). The red and green cylinders indicate tumor and control samples' extraction sites respectively. The extracted specimens had a volume of approximately 1 cm^3. Hematoxylin and eosin stained tissue. (D) high grade malignant epithelioid neoplasm producing malignant osteoid infiltrating the host bone trabeculae, consistent with high-grade osteoblastic osteosarcoma. Viable cells are shown. (E) low grade malignant spindle cells neoplasm associated with parallel-aligned bony trabeculae, consistent with low grade paraosteal osteosarcoma. (F) low grade periosteal osteosarcoma composed of lobules with low to intermediate grade cartilaginous component. Hypercellular areas are visible on the top of the picture.

inspected with the open-source software Fiji [20] and 3D visualizations were realized using the commercial software Amira (Thermo Fisher Scientific, Waltham, MA, USA).

2.4.2. X-ray fluorescence microscopy and micro- X-ray absorption near-edge spectroscopy

2D X-ray fluorescence microscopy maps and single point μ–X-ray Absorption Near Edge Spectroscopy spectra were acquired at the ID21 beamline of the ESRF (Grenoble, France) [21]. The beam was focused to ~0.4 × 0.9 (VxH) μm^2 with a Kirkpatrick-Baez (KB) mirror system. The energy selection was done using a double crystal fixed exit monochromator equipped with Si 111 crystals. The emitted fluorescence signal was detected with an energy-dispersive large area (80 mm^2) SDD detector (SGX from RaySpec).

After embedding the bone blocks in PMMA, thin sections, approximately 90–100 μm thick, were cut using a diamond saw and mounted in the sample holder, clamped between two polymer films. XRFM maps were acquired at an energy of 4.3 keV, corresponding to the Ca K-edge region. Elements with lower absorption edge energies were also excited, allowing simultaneous mapping of Ca, P, and K. Fluorescence maps were obtained with step sizes of 5 μm and 1 μm to identify bone tissue. XANES spectra were then collected at a pixel size of 1 μm in points of interest identified from the fluorescence maps, with the incident beam energy being varied between 4.02 keV and 4.17 keV at 0.3 eV steps. Elemental peak deconvolution of the fluorescence maps was carried out using the data analysis tool PyMCA [22]. μXANES spectra were normalized and analyzed with both PyMCA and Orange [23]. Principal Component Analysis (PCA) performed with Orange, was used to classify the spectra based on their main spectral features. PCA is a dimensionality reduction technique that identifies the principal components (or directions of greatest variance) within a dataset. In our analysis, the technique was used to reduce the complexity of the spectral data and to identify underlying patterns and groupings based on the spectral features.

2.4.3. X-ray diffraction

Thin sections of PMMA-embedded bone blocks ranging from 50 to 70 μm were mounted onto microscope slides. XRD measurements were conducted on the XRD1 beamline at the Elettra Synchrotron Radiation Facility (Trieste, Italy). The beam energy was set to 12.3984 keV (wavelength 1 Å) using a vertical collimating mirror and a double-crystal Si (111) monochromator, followed by a bendable focusing mirror that directed the beam onto the sample. The diffracted signal was recorded by a 2D detector (Dectris Pilatus 2M) with 1475 × 1679 pixels of 172 × 172 μm^2. The sample-to-detector distance was set to 200 mm, and LaB6 powder X-ray diffraction was used to calibrate the collected patterns. Beam dimension, obtained by means of a pinhole, was kept at 50 μm. Typical XRD profiles for each sample are shown in Fig. S3. Scanning diffraction with a resolution of 100 μm in both directions was performed in transmission mode over regions of interest (ROIs) of the sample to study the distribution of HA within the selected areas. The ROIs selection was performed by comparing the analyzed sampled to adjacent histology sections. Bidimensional patterns integration was performed using the software Fit2d (U.K.: http://www.ccp14.ac.uk/ccp/web-mirrors/fit2d/computing/scientific/FIT2D/). The integrated intensity and full width at half maximum (FWHM) of the 002 peak were extracted from peaks normalized against the background. From the peak's intensities, a colormap was created, illustrating the spatial distribution of the detected HA integrated intensity with the resolution of the XRD scan (100 μm). The radial data integration of the signal allowed to analyze the c-axis of the HA crystals in control and tumoral bone by calculating the d-spacing (interplanar distance) of the 002 reflection [24].

2.5. Statistical analysis

The frequency distributions of the HA interplanar distances in control and tumor samples were plotted and analyzed using GraphPad Prism 10.0.2 (GraphPad Software, San Diego, CA, USA). To assess whether statistically significant differences existed between control and tumor bone for each osteosarcoma subtype, a Student's t-test was performed. A p-value of < 0.05 was considered statistically significant.

3. Results

This work aimed to provide new insights into osteosarcoma through a comprehensive multiscale characterization of the mineral component of the tumor microenvironment. Three human osteosarcoma samples were analyzed using the following X-ray synchrotron-based techniques: X-ray computed micro tomography, X-ray absorption near edge spectroscopy and X-ray diffraction. Samples were isolated from tissues obtained after surgical resection of high-grade osteoblastic sarcoma, parosteal and periosteal OS (Fig. 1). To avoid the chance of tumor local recurrence, OS were resected with wide margins. For each patient a region not affected by the tumor was used as internal control. The region from which the control and tumoral samples were obtained has been indicated in Fig. 1.

3.1. Multimodal and multiscale characterization of the tumor microenvironment

To evaluate the 3D morphology of tumor and control bone tissue, we exploited the high spatial and contrast resolution of XCmT to discriminate fine microstructural details and phases with close refraction indices [25]. For each sample, tomographic acquisitions were performed in different regions of the resected tissue to account for intrasubject variability of bone tissue morphology. A qualitative comparison of 3D reconstructions revealed a reduction in trabecular bone volume compared to the control tissue (Fig. 2 A and B), with mean bone volume decreasing from 13.5 % in control to 10.7 % in HG-OS. The tumoral region of HG-OS (Fig. 2 C) exhibited trabecular shrinkage, disrupted bone edges, and irregular morphology (white arrows), whereas the control sample (Fig. 2 D) maintained a more homogeneous structure.

In the PA-OS, the tumor tissue appeared morphologically heterogeneous (Fig. 2 E) compared to the control (Fig. 2 F). In fact, this type of tumor originated from the outer layer of the periosteum [26] generating a lobulated and exophytic mass with central dense ossification adjacent to the bone. The reconstructed volumes (Fig. 2 G–I) further revealed cortical thickening and mineralization within the external mass, where abnormal trabeculae are clearly distinguishable. The PE-OS, which arises from the inner periosteal layer, is characterized by a predominant cartilaginous component with osteolytic features compatible with streamers of lytic bone matrix [26]. This is evident in Fig. 2 L, where osteolytic lesions appear, with the mineral component primarily consisting of hypo-mineralized bone, in contrast to the denser control tissue observed in Fig. 2 M. Additionally, a tomographic slice in Fig. 2 N provides further insight into the altered structural organization within the PE-OS sample.

After delineating the 3D structure of the sample, bone samples were embedded in PMMA and cut into serial sections as described in the Methods paragraph (Section 2.2). Sections of 100–150 μm were stained with Stevenel's blue – Van Gieson staining to depict the tissue composition and bone morphology (see Fig. S2). Adjacent sections were analyzed by μXANES combined with X-ray fluorescence microscopy, and XRD. The staining allowed to visualize the trabecular or compact mineralized bone in red-orange, while bone marrow, osteoid matrix and cellular components were stained in shades of blue. Interestingly, histological analysis confirmed the results obtained by tomographic acquisitions. HG-OS trabecular bone showed areas of bone disruption and tumor-damaged tissue (red arrow in Fig. S2 A), compared to control tissue, where bone tissue edges appeared regular and homogeneous. In the PA-OS, the tumor tissue appeared morphologically heterogeneous, with densely ossified and lobulated mass (red arrows in Fig. S2 B) and

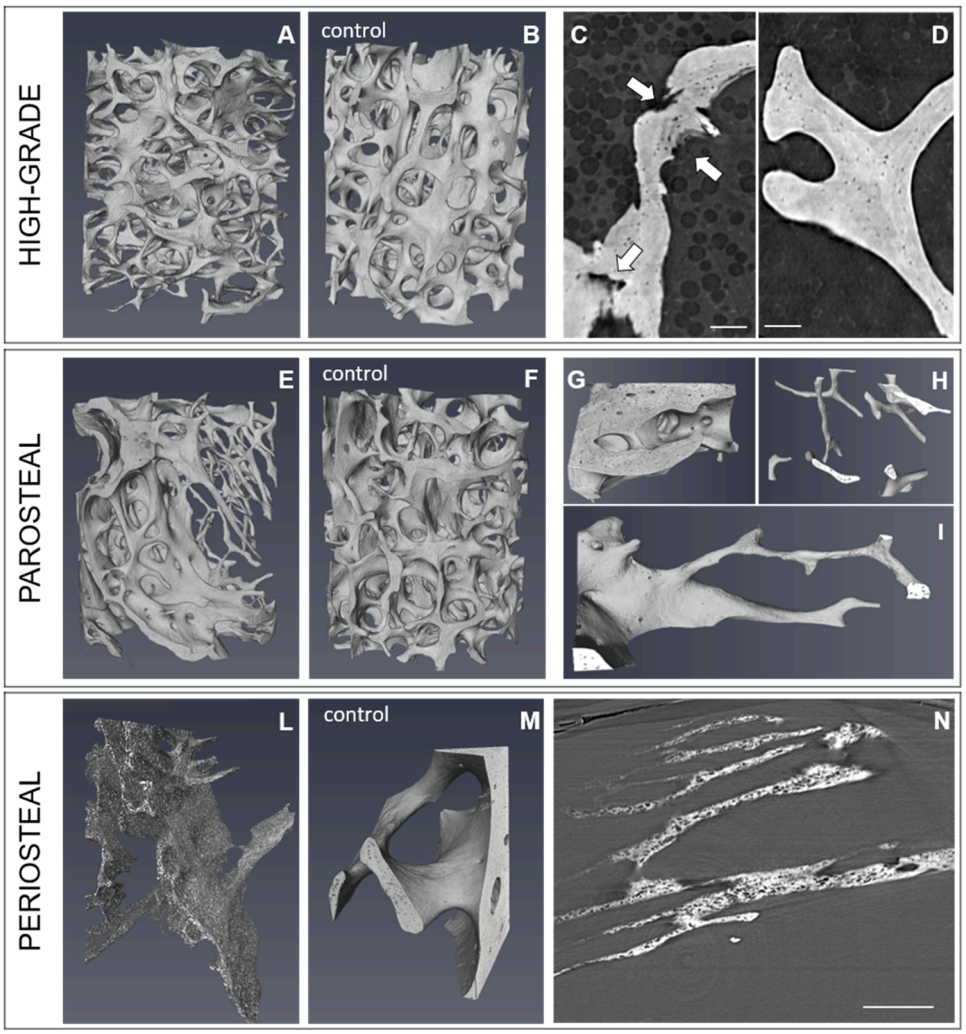

Fig. 2. In (A) and (B), 3D renderings of tumoral and control HG-OS (isotropic voxel size 2.0 μm, the dimension of the analyzed volumes is approximately 64 mm^3) are showed. Bone damage can be appreciated by comparing the virtual sections in (C) and (D) acquired with an isotropic voxel size of 0.9 μm, representing, respectively, tumoral and control HG-OS samples. The white arrows indicate damaged regions (scale bar 100 μm). In (E) and (F), 3D renderings of tumoral and control PA-OS (voxel size 2.0 μm, volume analyzed approximately 64 mm^3) are reported, while from (G) to (I) volumes were acquired in different regions of (E) (voxel size 0.9 μm, volumes analyzed approximately 8 mm^3). (L) and (M) show 3D renderings of tumoral and control PE-OS, (voxel size 0.9 μm, volumes analyzed approximately 8 mm^3) while N shows a virtual section acquired from tumoral PE-OS with a voxel size of 0.9 μm (scale bar 0.25 mm).

atypical spindle cells (red circle in Fig. S2 B) between the osseous trabeculae. In contrast, control PA-OS samples appeared mineralized, displaying both trabecular and cortical bone structures Fig. S2 B). Finally, the PE-OS histological analysis reported in Fig. 2 C highlighted the presence of lobular and cartilaginous tissue, separated by malignant appearing spindle cells. PE-OS is indeed a type of OS arising from the inner layer of the periosteum and is primarily a chondroblastic tumor (composed mostly of cartilaginous tissue), producing osteoid or bone. Osteoid production by neoplastic cells was visible (red arrows in Fig. S2 C), and dense areas of calcification were detected. Control PE-OS samples showed well-mineralized cortical bone with visible osteons, reflecting an organized bone structure (Fig. S2 C).

XRFM was used to specifically locate bone tissue within each sample revealing its elemental composition (P, K, Ca) at the micrometric scale. From the XRFM maps, points of interest were selected for the acquisition of Ca K-edge XANES spectra, a well-established technique that allows to characterize the chemical state of mineral bone tissue providing information about the atoms surrounding the calcium ion. To investigate whether a difference between the spectroscopic data acquired from control and tumoral samples existed, unsupervised principal component analysis (PCA) was used. The score PC1 vs PC2 scatter plot in Fig. 3 A showed two separated clusters (blue and red regions respectively). Spectra in the blue region (Fig. 3 A) were acquired from control samples and tumoral HG-OS. The mean spectrum corresponding to this region is shown in Fig. 3 B (blue mean spectrum - data 1) and reveals that there are no differences in the chemical state of calcium between the control and the tumoral HG-OS. It is worth noting that this cluster also included the HA reference, a calcium phosphate compound that is the main mineral component of healthy bone tissue [27,28]. A typical HA Ca K-edge spectrum presents a main absorption peak (Fig. S4, letter C), called white line, a pre-edge (Fig. S4, letter A), a shoulder preceding the white line (Fig. S4, letter B) and oscillation peaks at higher energies (see Fig. S4, letters D to H) [29,30]. The red region in Fig. 3 A contained spectra acquired from the tumor PE-OS and PA-OS, showing different spectral features compared to the HA reference and the mean spectrum representing the control bone tissue. These spectra lacked the shoulder before the white line and appeared less steep in the region after the main absorption peak, suggesting the presence of amorphous calcium carbonate (ACC) after a comparison with reference spectra available in literature [31] (Fig. 3 B, mean red spectrum - data 2). To localize the ACC, the high spatial resolution and sensitivity of the XRFM was used. All the ACC spectra were observed to belong to small mineral nuclei of

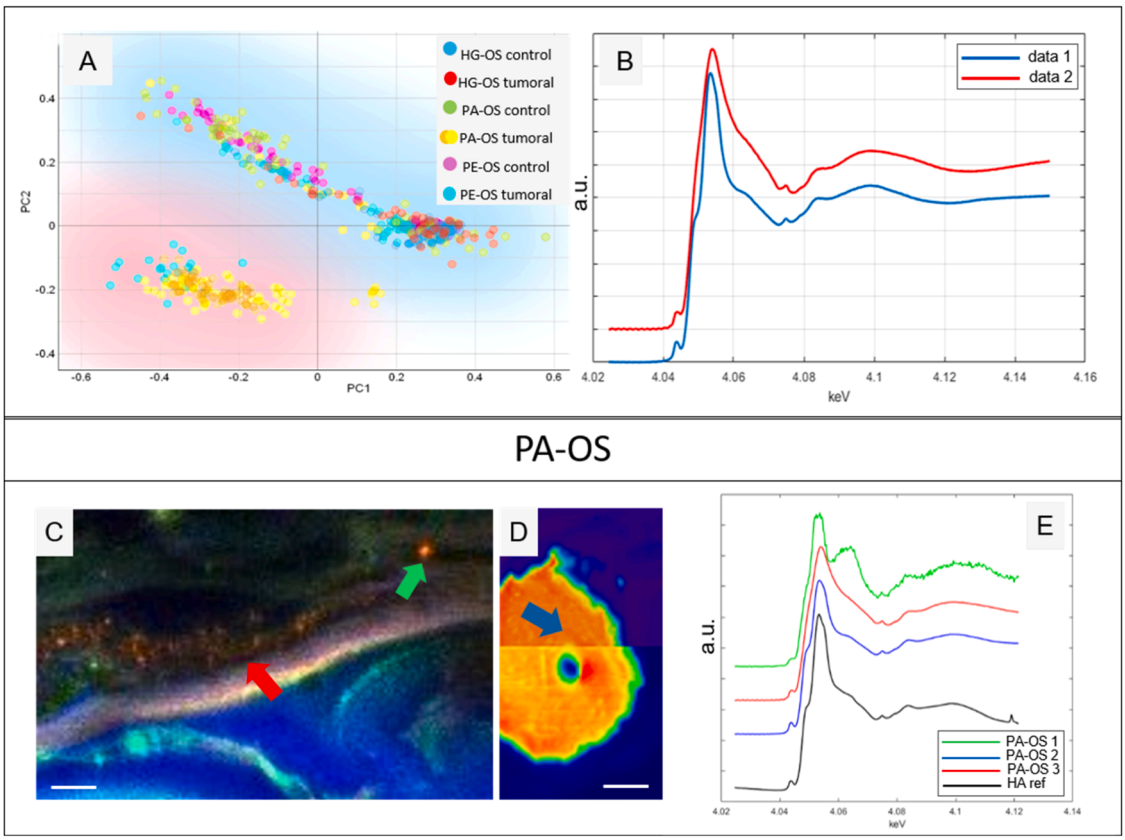

Fig. 3. PCA analysis results. In (A) the score PC1 vs PC2 scatter plot shows two separate clusters (blue and red regions). (B) reports the mean spectrum derived from the blue (spectrum corresponding to "data 1") and the red regions (spectrum corresponding to "data 2"). The XRFM map of sample PA-OS is provided in (C) (red = calcium, blue = phosphorus, green = potassium) and (D) (only calcium is displayed), scale bar is 0.2 mm. (E) reports spectra acquired from points in (C) and (D) indicated with arrows. The green spectrum (PA-OS 1) represents a calcium carbonate compound (green arrow in C), the blue spectrum (PA-OS 2) was acquired from structured bone tissue (blue arrow in D) and the red spectrum (PA-OS 3) belongs to non-structured bone tissue (red arrow in C). The HA reference is reported in black.

non-structured bone tissue (Figs. S5 A, 3 C and E, ACC spectrum in red). These mineral precipitates were not detectable using standard histological staining methods (see supplementary information, Fig. S2), likely due to the limited sensitivity of these techniques in identifying early-stage mineral nuclei or amorphous calcium compounds. This highlights the utility of synchrotron-based X-ray techniques in revealing sub-micrometer details of the tumor microenvironment. Interestingly, a calcium carbonate spectrum was also observed (green arrow in Fig. 3 C and E, green spectrum). In the same regions, XRFM showed well-defined P and K fluorescence maps suggesting the presence of an organized cellular organic matrix (Fig. 3 C). On the other hand, in structured bone tissue (Fig. 3 D), spectra (Fig. 3 E, blue spectrum) were more similar to the HA reference and belonged to the light-blue region in Fig. 3 A (Fig. 3 B, blue spectrum - data 1). In Fig. S5, we provide XRFM maps of PA-OS (Fig. S5 A, B), HG-OS (Fig. S5 C, D), and PE-OS (Fig. S5 E, F), overlaid with light-microscope images of the analyzed samples. Notably, the observed morphological features align with the findings from both tomography (Fig. 2) and histology (Fig. S2).

X-ray diffraction played a crucial role in understanding the structural properties of bone by providing insights into the HA distribution in the samples. The technique allowed mapping the local density of the HA which is part of the mineral phase of bone [32]. We focused on the 002-diffraction peak, which corresponds to the longitudinal axis of the plate-like HA crystals, to characterize the mineral component in bone tissue under both physiological and pathological conditions [33]. For each sample, the spatial mapping of the 002 HA diffraction peak integrated intensity was assessed, providing a quantitative evaluation of the amount of crystalline mineral phase locally present (Fig. S6) in the regions of interest individuated in each control and tumoral bone tissue. The plots in Fig. 4 A–C represent the FWHM of the 002 HA peak as a function of its intensity. All plots highlight the presence of two clusters representing two different structural phases, one indicating a lower crystallinity (high FWHM) and the other representing a higher crystallinity (low FWHM). In all samples, both clusters contained values acquired from both control and tumoral tissues. The distribution of the HA crystals' interplanar distance was analyzed to assess differences in the hydroxyapatite c-axis between control and tumor-associated bone (Fig. 4 D–F). These distortions in the HA crystal lattice may result from structural defects that modify atomic spacing and alter the angles between crystallographic planes, potentially impacting the material's properties. The distributions derived from the control and the tumoral HG-OS had comparable means (Fig. 4 D, respectively yellow and orange lines). On the other side, the PE-OS and the PA-OS showed significantly different distributions ($p < 0.01$, Fig. 4 E and F), indicative of a less ordered and more oriented crystalline organization in tumoral samples compared to controls.

4. Discussion

In this study, we investigated the osteosarcoma tumor microenvironment by examining tissue resected from three distinct osteosarcomas: osteoblastic, parosteal, and periosteal. We employed advanced X-ray synchrotron-based techniques to conduct a comprehensive multiscale analysis ranging from several millimeters to the atomic scale. Our main findings revealed significant morphological inhomogeneities among the three osteosarcomas, while confirming that the biomineralization process remains active in all samples, as evidenced by HA crystal formation in both control and tumor tissues. Indeed, XRD showed two

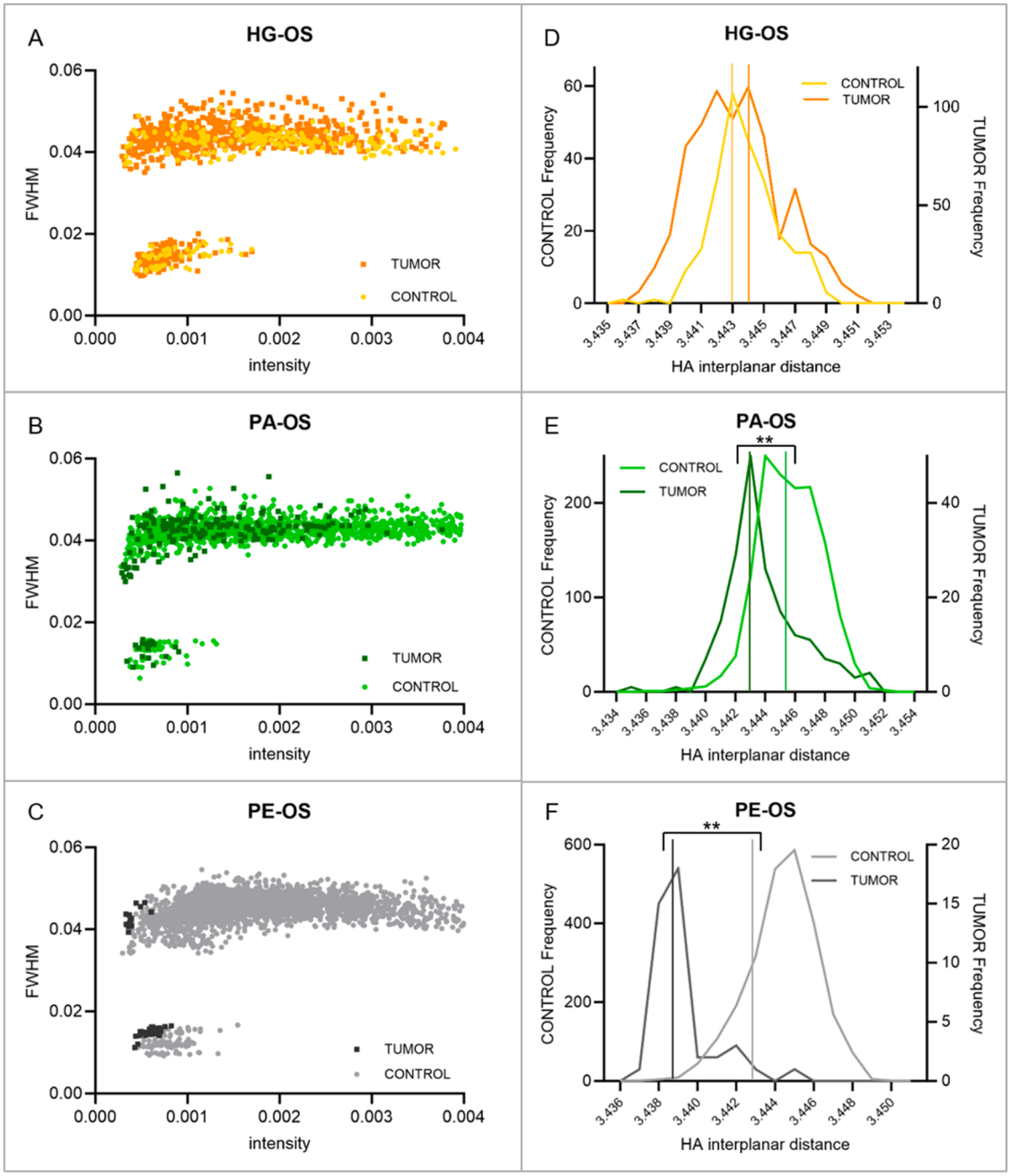

Fig. 4. Scatter plot of the FWHM as function of the integrated intensity from HG-OS (A), PA-OS (B) and PE-OS (C). Frequency distribution of the HA crystals' interplanar distance of HG-OS (D), PA-OS (E) and PE-OS (F). The y-axis represents the frequency of the HA measured interplanar distances. Vertical lines indicate the mean values of each distribution (orange line = 3.44476 Å, yellow line = 3.44384 Å, dark-green line = 3.44344 Å, green line = 3.44586 Å, black line = 3.43917 Å, gray line = 3.44317 Å). Student's t-test was performed: * $p < 0.05$, ** $p < 0.01$, ***$p < 0.001$.

crystalline phases of HA in all control and tumor resections (Fig. 4 A–C), corresponding to high crystallinity (HC-HA) and low crystallinity (LC-HA) of the HA. A simplistic explanation might attribute the HC-HA to older, compact bone and LC-HA to bone undergoing remodeling and turnover. However, our results suggest a more complex phenomenon beyond this binary classification. Criticality [13], a property observed in phase transitions of matter, constitutes a possible framework for understanding the observed coexistence of HC- and LC-HA phases. Similar features have been identified in biological systems like the brain, where structural organization follows critical-state dynamics [14]. Extending this concept to bone suggests that its mineralization may operate near a critical point where shifts in hydroxyapatite mineralization may occur, even in pathological states such as osteosarcoma. The consistent presence of these two crystallinity phases across both healthy and pathological tissues suggests that this coexistence may be an intrinsic property of the biomineralization process itself.

However, the HA crystal structure in the PA-OS and the PE-OS is misshaped compared to healthy control bone, while it is the same in the control and tumor HG-OS (Fig. 4 D–F). These deformations found in PA-OS and PE-OS correspond to a shortened length of the HA crystal along the crystal c-axis, corresponding to the direction along the collagen fibers [27]. A similar result was derived by Zanghellini et al. [34] in a sclerosing osteosarcoma, a rare subtype of bone tumor, and in a parosteal osteosarcoma [24]. They observed a clear contraction of the HA c-axis in tumor tissue which was attributed to lower A-type carbonate substitutions [35]. It is known that bone mineral is composed of a mixed

A- and B-type of HA, with a higher amount of B type [36]. Therefore, these results suggest that there is a shift towards A-type HA in newly formed bone of the PA-OS and the PE-OS. Besides consideration of HA on the three different tumors, the μXANES results provided a deeper understanding of the biomineralization process. The most striking result was that in the PA-OS and the PE-OS altered biomineralization was observed, while in HG-OS the tumor bone was comparable to the HG-OS control bone. In particular, the HG-OS was the only tumor showing a mature HA without other calcium-containing minerals (as confirmed by PCA analysis in Fig. 3 A and B) such as calcite and other types of calcium compounds [37–39]. On the other hand, the PA-OS and the PE-OS showed a heterogeneous scenario with HA present in neo-formed exophytic tumor tissue together with minerals of crystalline and amorphous calcium carbonate (spectra in Fig. 3 E).

At present, OS literature concerning the characterization of the TME in different OS subtypes is relatively scarce. Indeed, this scarcity can be partly attributed to the fact that OS is a rare heterogeneous disease affecting a low percentage of subjects and partly to the challenges associated to the availability of bone resected tissue for research purposes. Within this scenario, some limitations can be identified. While synchrotron radiation techniques ensure high resolution and multiscale analysis, they significantly limit the number of samples that can be analyzed in a single experiment. In this study, one representative case per OS subtype was analyzed at a single time point, limiting the transferability of our findings to broader clinical contexts. While this approach has allowed us to investigate three distinct OS subtypes in depth using a comprehensive multiscale strategy, further studies in a larger cohort of patients are essential to confirm these findings and fully characterize the mineralization features observed. OS is often diagnosed at advanced stages through radiography, with surgical resection being the main treatment option and the principal source of viable tissue. Accordingly, our samples were obtained from residual material after tumour removal, reflecting the state of the tissue at the time of surgery. Despite these limitations, the integration of multiple techniques on the same specimen provided new and detailed insights into local bone pathology. Notably, this study stands out for the analysis of multiple osteosarcoma subtypes using cutting-edge synchrotron radiation techniques and their comparison to the corresponding control tissue, providing a unique and detailed characterization of tumor-associated bone across different pathological variants. By revealing significant variations in HA crystallinity and tumor bone mineral composition and morphology, the research supports the idea that osteosarcoma affects mineralized bone tissue in a complex, heterogeneous manner. We acknowledge that mineralization alone does not comprehensively characterize disease progression, as multiple interacting biological components, including stromal, vascular, and immune cells, contribute to tumor development. However, our research focuses on understanding the structural and mineral characteristics of different OS subtypes, essential for a better comprehension of osteosarcoma complexity and heterogeneity. One important application of this study is in the development of 3D *in vitro* models, which can be extended to patient-derived OS cell models for use in personalized medicine. By accurately replicating the OS TME *in vitro*, these models could facilitate drug testing and the identification of patient-specific therapeutic responses.

The insights provided in this work enhance our understanding of osteosarcoma's impact on bone tissue, emphasizing the need to further investigate the dynamic interactions within the tumor microenvironment.

Funding

The research was funded by MUR (Ministero dell'Università e della Ricerca) PRIN22 (2022WKNWRF_001 - CUP J53D23006280006).

CRediT authorship contribution statement

Francesca Rossi: Writing – review & editing, Writing – original draft, Visualization, Validation, Supervision, Software, Resources, Project administration, Methodology, Investigation, Formal analysis, Data curation, Conceptualization. **Martyna Malgorzata Rydzyk:** Writing – review & editing, Project administration, Investigation, Formal analysis, Data curation. **Luisa Barba:** Writing – review & editing, Writing – original draft, Validation, Software, Methodology, Investigation, Formal analysis, Data curation. **Emil Malucelli:** Writing – review & editing, Writing – original draft, Visualization, Validation, Supervision, Software, Project administration, Methodology, Investigation, Funding acquisition, Formal analysis, Data curation, Conceptualization. **Maria Elisabetta Federica Palamà:** Writing – review & editing, Writing – original draft, Visualization, Validation, Software, Methodology, Investigation, Formal analysis, Data curation. **Chiara Gentili:** Writing – review & editing, Writing – original draft, Resources, Project administration, Methodology, Funding acquisition, Conceptualization. **Maddalena Mastrogiacomo:** Writing – review & editing, Supervision, Conceptualization. **Alessia Cedola:** Writing – review & editing, Validation, Supervision. **Lucia Mancini:** Writing – review & editing, Writing – original draft, Supervision, Software, Methodology, Investigation, Formal analysis, Data curation. **Murielle Salomé:** Writing – review & editing, Writing – original draft, Software, Project administration, Methodology, Investigation, Formal analysis, Data curation. **Hiram Castillo-Michel:** Writing – review & editing, Writing – original draft, Validation, Software, Methodology, Investigation, Data curation. **Davide Maria Donati:** Writing – review & editing, Resources. **Marco Gambarotti:** Writing – review & editing, Resources. **Enrico Lucarelli:** Writing – review & editing, Writing – original draft, Supervision, Resources, Methodology, Conceptualization. **Michela Fratini:** Writing – review & editing, Writing – original draft, Visualization, Validation, Supervision, Software, Project administration, Methodology, Investigation, Formal analysis, Data curation, Conceptualization. **Stefano Iotti:** Writing – review & editing, Writing – original draft, Visualization, Supervision, Project administration, Conceptualization.

Declaration of competing interest

The authors declare that they have no known competing financial interests or personal relationships that could have appeared to influence the work reported in this paper.

Acknowledgments

Beamtime provided by the Elettra synchrotron at the SYRMEP (proposal 20200272 - doi.org/10.34965/I11158) and XRD1 (proposals 20220491 and 20205428 - doi.org/10.34965/i9312 and doi.org/10.34965/i10486) beamlines is gratefully acknowledged. We also thank the ESRF for beamtime at the ID21 beamline under proposal LS-3202 (doi.org/10.15151/ESRF-ES-1229952144).

Supplementary materials

Supplementary material associated with this article can be found, in the online version, at doi:10.1016/j.actbio.2025.04.057.

References

[1] H.C. Beird, S.S. Bielack, A.M. Flanagan, J. Gill, D. Heymann, K.A. Janeway, J. A. Livingston, R.D. Roberts, S.J. Strauss, R. Gorlick, Osteosarcoma, Nat. Rev. Dis. Prim. 8 (2022) 1–19, https://doi.org/10.1038/s41572-022-00409-y, 2022 8:1.
[2] J. Gill, R. Gorlick, Advancing therapy for osteosarcoma, Nat. Rev. Clin. Oncol. 18 (2021) 609–624, https://doi.org/10.1038/s41571-021-00519-8, 2021 18:10.
[3] I. Corre, F. Verrecchia, V. Crenn, F. Redini, V. Trichet, The osteosarcoma microenvironment: a complex but targetable ecosystem, Cells 9 (2020), https://doi.org/10.3390/CELLS9040976.

[4] Z. Shoaib, T.M. Fan, J.M.K. Irudayaraj, Osteosarcoma mechanobiology and therapeutic targets, Br. J. Pharmacol. 179 (2022) 201–217, https://doi.org/10.1111/BPH.15713.

[5] H.K. Brown, K. Schiavone, F. Gouin, M.F. Heymann, D. Heymann, Biology of bone sarcomas and new therapeutic developments, Calcif. Tissue Int. 102 (2017) 174–195, https://doi.org/10.1007/S00223-017-0372-2, 2017 102:2.

[6] E.P. Young, A.E. Marinoff, E. Lopez-Fuentes, E.A. Sweet-Cordero, Osteosarcoma through the lens of bone development, signaling, and microenvironment, Cold Spring Harb. Perspect. Med. 14 (2024) a041635, https://doi.org/10.1101/CSHPERSPECT.A041635.

[7] H. Zhang, T. Wang, H. Gong, R. Jiang, W. Zhou, H. Sun, R. Huang, Y. Wang, Z. Wu, W. Xu, Z. Li, Q. Huang, X. Cai, Z. Lin, J. Hu, Q. Jia, C. Ye, H. Wei, J. Xiao, A novel molecular classification method for osteosarcoma based on tumor cell differentiation trajectories, Bone Res. 11 (2023) 1–15, https://doi.org/10.1038/s41413-022-00233-w, 2023 11:1.

[8] Y. Liu, D. Luo, T. Wang, Hierarchical structures of bone and bioinspired bone tissue engineering, Small 12 (2016) 4611–4632, https://doi.org/10.1002/SMLL.201600626.

[9] M.E. Launey, M.J. Buehler, R.O. Ritchie, On the mechanistic origins of toughness in bone, Annu. Rev. Mater. Res. 40 (2010) 25–53, https://doi.org/10.1146/ANNUREV-MATSCI-070909-104427/CITE/REFWORKS.

[10] E.A. Zimmermann, R.O. Ritchie, Bone as a structural material, Adv. Healthc. Mater. 4 (2015) 1287–1304, https://doi.org/10.1002/ADHM.201500070.

[11] T. Magrini, R. Libanori, A. Kan, A.R. Studart, Complex materials: the tough life of bone, Rev. Bras. Ensino Fís. 43 (2021) e20200438, https://doi.org/10.1590/1806-9126-RBEF-2020-0438.

[12] N. Reznikov, M. Bilton, L. Lari, M.M. Stevens, R. Kröger, Fractal-like hierarchical organization of bone begins at the nanoscale, Science 360 (2018), https://doi.org/10.1126/SCIENCE.AAO2189/SUPPL_FILE/AAO2189S4.MP4 (1979).

[13] M.A. Muñoz, Colloquium: criticality and dynamical scaling in living systems, Rev. Mod. Phys. 90 (2018) 031001, https://doi.org/10.1103/REVMODPHYS.90.031001/FIGURES/6/MEDIUM.

[14] H.S. Ansell, I.A. Kovács, Unveiling universal aspects of the cellular anatomy of the brain, Commun. Phys. 7 (2024) 1–11, https://doi.org/10.1038/s42005-024-01665-y, 2024 7:1.

[15] G. Werner, Fractals in the nervous system: conceptual implications for theoretical neuroscience, Front. Physiol. (2010) 1787, https://doi.org/10.3389/FPHYS.2010.00015/BIBTEX, 1 JUL.

[16] A. Abrami, F. Arfelli, R.C. Barroso, A. Bergamaschi, F. Billè, P. Bregant, F. Brizzi, K. Casarin, E. Castelli, V. Chenda, L. Dalla Palma, D. Dreossi, C. Fava, R. Longo, L. Mancini, R.H. Menk, F. Montanari, A. Olivo, S. Pani, A. Pillon, E. Quai, S. R. Kaiser, L. Rigon, T. Rokvic, M. Tonutti, G. Tromba, A. Vascotto, C. Venanzi, F. Zanconati, A. Zanetti, F. Zanini, Medical applications of synchrotron radiation at the SYRMEP beamline of ELETTRA, Nucl. Instrum. Methods Phys. Res. A 548 (2005) 221–227, https://doi.org/10.1016/J.NIMA.2005.03.093.

[17] A. Mittone, L. Fardin, F. Di Lillo, M. Fratini, H. Requardt, A. Mauro, R.A. Homs-Regojo, P.A. Douissard, G.E. Barbone, J. Stroebel, M. Romano, L. Massimi, G. Begani-Provinciali, F. Palermo, S. Bayat, A. Cedola, P. Coang, A. Bravin, Multiscale pink-beam microCT imaging at the ESRF-ID17 biomedical beamline, J. Synchrotron. Radiat. 27 (2020) 1347–1357, https://doi.org/10.1107/S160057752000911X.

[18] F. Brun, L. Massimi, M. Fratini, D. Dreossi, F. Billé, A. Accardo, R. Pugliese, A. Cedola, SYRMEP Tomo project: a graphical user interface for customizing CT reconstruction workflows, Adv. Struct. Chem. Imaging 3 (2017), https://doi.org/10.1186/S40679-016-0036-8.

[19] F. Brun, S. Pacilè, A. Accardo, G. Kourousias, D. Dreossi, L. Mancini, G. Tromba, R. Pugliese, Enhanced and flexible software tools for X-ray computed tomography at the Italian synchrotron radiation facility elettra, Fundam. Inform. 141 (2015) 233–243, https://doi.org/10.3233/FI-2015-1273.

[20] J. Schindelin, I. Arganda-Carreras, E. Frise, V. Kaynig, M. Longair, T. Pietzsch, S. Preibisch, C. Rueden, S. Saalfeld, B. Schmid, J.Y. Tinevez, D.J. White, V. Hartenstein, K. Eliceiri, P. Tomancak, A. Cardona, Fiji: an open-source platform for biological-image analysis, Nat. Methods 9 (2012) 676–682, https://doi.org/10.1038/nmeth.2019, 2012 9:7.

[21] M. Cotte, E. Pouyet, M. Salomé, C. Rivard, W. De Nolf, H. Castillo-Michel, T. Fabris, L. Monico, K. Janssens, T. Wang, P. Sciau, L. Verger, L. Cormier, O. Dargaud, E. Brun, D. Bugnazet, B. Fayard, B. Hesse, A.E. Pradas Del Real, G. Veronesi, J. Langlois, N. Balcar, Y. Vandenberghe, V.A. Solé, J. Kieffer, R. Barrett, C. Cohen, C. Cornu, R. Baker, E. Gagliardini, E. Papillon, J. Susini, The ID21 X-ray and infrared microscopy beamline at the ESRF: status and recent applications to artistic materials, J. Anal. At. Spectrom. 32 (2017) 477–493, https://doi.org/10.1039/C6JA00356G.

[22] V.A. Solé, E. Papillon, M. Cotte, P. Walter, J. Susini, A multiplatform code for the analysis of energy-dispersive X-ray fluorescence spectra, Spectrochim. Acta Part B At. Spectrosc. 62 (2007) 63–68, https://doi.org/10.1016/J.SAB.2006.12.002.

[23] J. Demšar, T. Curk, A. Erjavec, Č. Gorup, T. Hočevar, M. Milutinovič, M. Možina, M. Polajnar, M. Toplak, A. Starič, M. Štajdohar, L. Umek, L. Žagar, J. Žbontar, M. Žitnik, B. Zupan, Orange: data mining toolbox in Python, J. Mach. Learn. Res. 14 (2013) 2349–2353. http://jmlr.org/papers/v14/demsar13a.html. accessed January 29, 2024.

[24] B. Zanghellini, N. Zechmann, D. Baurecht, T.A. Grünewald, M. Burghammer, B. Liegl-Atzwanger, A. Leithner, A. Davydok, H. Lichtenegger, Multimodal analysis and comparison of stoichiometric and structural characteristics of parosteal and conventional osteosarcoma with massive sclerosis in human bone, J. Struct. Biol. 216 (2024) 108106, https://doi.org/10.1016/J.JSB.2024.108106.

[25] S. Ma, O. Boughton, A. Karunaratne, A. Jin, J. Cobb, U. Hansen, R. Abel, Synchrotron imaging assessment of bone quality, Clin. Rev. Bone Miner. Metab. 14 (2016) 150, https://doi.org/10.1007/S12018-016-9223-3.

[26] G. Yarmish, M.J. Klein, J. Landa, R.A. Lefkowitz, S. Hwang, Imaging characteristics of primary osteosarcoma: nonconventional subtypes, Radiographics 30 (6) (2010) 1653–1672, https://doi.org/10.1148/RG.306105524.

[27] B. Wang, Z. Zhang, H. Pan, Bone apatite nanocrystal: crystalline structure, chemical composition, and architecture, Biomimetics 8 (2023) 90, https://doi.org/10.3390/BIOMIMETICS8010090/S1.

[28] A. Ressler, A. Žužić, I. Ivanišević, N. Kamboj, H. Ivanković, Ionic substituted hydroxyapatite for bone regeneration applications: a review, Open Ceram. 6 (2021) 100122, https://doi.org/10.1016/J.OCERAM.2021.100122.

[29] D. Eichert, M. Salomé, M. Banu, J. Susini, C. Rey, Preliminary characterization of calcium chemical environment in apatitic and non-apatitic calcium phosphates of biological interest by X-ray absorption spectroscopy, Spectrochim. Acta Part B At. Spectrosc. 60 (2005) 850–858, https://doi.org/10.1016/J.SAB.2005.05.012.

[30] B. Hesse, M. Salome, H. Castillo-Michel, M. Cotte, B. Fayard, C.J. Sahle, W. De Nolf, J. Hradilova, A. Masic, B. Kanngießer, M. Bohner, P. Varga, K. Raum, S. Schrof, Full-field calcium K-edge X-ray absorption near-edge structure spectroscopy on cortical bone at the micron-scale: polarization effects reveal mineral orientation, Anal. Chem. 88 (2016) 3826–3835, https://doi.org/10.1021/ACS.ANALCHEM.5B04898/ASSET/IMAGES/LARGE/AC-2015-04898V_0008.JPEG.

[31] L. Monico, L. Cartechini, F. Rosi, W. De Nolf, M. Cotte, R. Vivani, C. Maurich, C. Miliani, Synchrotron radiation Ca K-edge 2D-XANES spectroscopy for studying the stratigraphic distribution of calcium-based consolidants applied in limestones, Sci. Rep. 10 (2020) 1–14, https://doi.org/10.1038/s41598-020-71105-8, 2020 10: 1.

[32] S. Tadano, B. Giri, X-ray diffraction as a promising tool to characterize bone nanocomposites, Sci. Technol. Adv. Mater. 12 (2012) 064708, https://doi.org/10.1088/1468-6996/12/6/064708.

[33] N. Sasaki, Y. Sudoh, X-ray pole figure analysis of apatite crystals and collagen molecules in bone, Calcif. Tissue Int. 60 (1997) 361–367, https://doi.org/10.1007/S002239900244/METRICS.

[34] B. Zanghellini, T.A. Grünewald, M. Burghammer, H. Rennhofer, B. Liegl-Atzwanger, A. Leithner, H.C. Lichtenegger, High-resolution large-area imaging of nanoscale structure and mineralization of a sclerosing osteosarcoma in human bone, J. Struct. Biol. 207 (2019) 56–66, https://doi.org/10.1016/J.JSB.2019.04.012.

[35] E.S. Kovaleva, M.P. Shabanov, V.I. Putlayev, Y.Y. Filippov, Y.D. Tretyakov, V. K. Ivanov, Carbonated hydroxyapatite nanopowders for preparation of bioresorbable materials, Mater. Werkst. 39 (2008) 822–829, https://doi.org/10.1002/MAWE.200800383.

[36] C. Rey, B. Collins, T. Goehl, I.R. Dickson, M.J. Glimcher, The carbonate environment in bone mineral: a resolution-enhanced fourier transform infrared spectroscopy study, Calcif. Tissue Int. 45 (1989) 157–164, https://doi.org/10.1007/BF02556059/METRICS.

[37] A. Procopio, E. Malucelli, A. Pacureanu, C. Cappadone, G. Farruggia, A. Sargenti, S. Castiglioni, D. Altamura, A. Sorrentino, C. Giannini, E. Pereiro, P. Cloetens, J.A. M. Maier, S. Iotti, Chemical fingerprint of Zn-hydroxyapatite in the early stages of osteogenic differentiation, ACS Cent. Sci. 5 (2019) 1449–1460, https://doi.org/10.1021/ACSCENTSCI.9B00509.

[38] A. Sorrentino, E. Malucelli, F. Rossi, C. Cappadone, G. Farruggia, C. Moscheni, A. J. Perez-Berna, J.J. Conesa, C. Colletti, N. Roveri, E. Pereiro, S. Iotti, Calcite as a precursor of hydroxyapatite in the early biomineralization of differentiating human bone-marrow mesenchymal stem cells, Int. J. Mol. Sci. 22 (2021), https://doi.org/10.3390/ijms22094939.

[39] F. Rossi, G. Picone, C. Cappadone, A. Sorrentino, M. Columbaro, G. Farruggia, E. Catelli, G. Sciutto, S. Prati, R. Oliete, A. Pasini, E. Pereiro, S. Iotti, E. Malucelli, Shedding light on osteosarcoma cell differentiation: impact on biomineralization and mitochondria morphology, Int. J. Mol. Sci. 24 (2023), https://doi.org/10.3390/IJMS24108559.